nuclear fusion
IAEA

PAPER • OPEN ACCESS

Growth, characterization and adhesion of thick deposited tungsten layers under transient loading in Magnum-PSI

To cite this article: T.W. Morgan *et al* 2026 *Nucl. Fusion* **66** 026051

OPEN ACCESS
IOP Publishing | International Atomic Energy Agency
Nuclear Fusion
Nucl. Fusion **66** (2026) 026051 (16pp)
https://doi.org/10.1088/1741-4326/ae34c5

Growth, characterization and adhesion of thick deposited tungsten layers under transient loading in Magnum-PSI

T.W. Morgan[1,2,*], L.J. Bouwmeester[2], L. Bana[3], M.J.H. Cornelissen[2,4], M. Rasinksi[5], E. Zoethout[1], J.A.G. van Kesteren[1,2], C.J.D. Robben[1,2], V. Mathayan[1], S. Brons[1], L.C.A. van Breemen[6], D. Dellasega[3,7], M. Passoni[3,7] and N. Lecis[8]

[1] DIFFER—Dutch Institute for Fundamental Energy Research, De Zaale 20, 5612 AJ Eindhoven, Netherlands
[2] Eindhoven University of Technology, Department of Applied Physics and Science Education, Groene Loper 19, 5612 Eindhoven, Netherlands
[3] Department of Energy, Politecnico di Milano, Via Lambruschini, 4, 20156 Milan, Italy
[4] Ecole Polytechnique Fédérale de Lausanne (EPFL), Swiss Plasma Center (SPC), CH-1015 Lausanne, Switzerland
[5] Forschungszentrum Jülich GmbH, Institut für Energie und Klimaforschung, 52425 Jülich, Germany
[6] Eindhoven University of Technology, Department of Mechanical engineering, De Rondom 70, 5612 AP Eindhoven, Netherlands
[7] Istituto per la Scienza e Tecnologia dei Plasmi, CNR, 20125 Milan, Italy
[8] Department of Mechanical Engineering, Via Privata G. La Masa 1, 20156 Milan, Italy

E-mail: t.w.morgan@differ.nl

Received 10 October 2025, revised 8 December 2025
Accepted for publication 7 January 2026
Published 23 January 2026

Abstract

The recent decision by ITER to move from a Be to a W first wall has significant implications for material transport and deposition, and can be expected to lead to increased W layer growth rate in deposition regions, which may flake leading to plasma disruption. In this work a novel sputtering set-up was implemented in the Magnum-PSI linear plasma device to create W layers under ITER relevant conditions. A W plate was inserted into the plasma edge and biased to cause sputtering of W in an Ar plasma. This sputtered W was entrained by the plasma and deposited on an array of mixed W and Mo targets at $<300\,^{\circ}\mathrm{C}$. The deposited layer thickness was later determined using weight gain of the targets, FIB-SEM cross sections and RBS. This showed a strongly inhomogeneous deposition profile with layer thicknesses varying from 100's nm up to $\geqslant 50\,\mu$m over a lateral region of around 3 cm diameter. Analysis of the layers by EDX, RBS, XRD and indentation testing showed them to be high purity dense W layers with mixed microstructure, forming columnular grains at greater thicknesses, with properties typical for W thin film growth. IR camera images showed flaking and delamination occurring during the deposition process, initiating at the layer-substrate interface and at imperfections or edges, with the flaking region growing over time. Films deposited on rough targets were better adhered than

* Author to whom any correspondence should be addressed.

on polished ones, and high deposition rates were more likely to lead to flaking. Subsequent loading of the grown layers under simultaneous D^+ plasma and ELM-like pulsed laser loading showed flaking to occur on previously adhered but poorly attached layers, as well as melt blobs forming at the edges of such layers. The results overall indicate that conditions in ITER should be favorable for growing well adhered layers, but that flaking may still occur and requires further evaluation.

Keywords: tungsten, erosion, re-deposition, flaking, thin film

(Some figures may appear in colour only in the online journal)

1. Introduction

Due to the recent choice by the ITER organization to change the first wall (FW) armor material of ITER from beryllium (Be) to tungsten (W), the surface area of W in the machine will be increased by a factor of ∼4, while at the same time prompt redeposition of eroded tungsten from the FW area will be significantly lower than can be expected in the divertor [1]. As a result, recent initial modeling indicates that, depending on the exact scenario, the total W erosion source from the FW may exceed that from the divertor by 1-3 orders of magnitude [2].

Dust production is commonly observed in metal walled machines such as JET [3, 4], AUG [5–7], EAST [8], C-Mod [9] and WEST [10] tokamaks, which is found to originate from molten metal droplets from disruptions, runaway electron melting events, or arcing, and from flaking of deposited layers. In the WEST tokamak, following the 2023 high-fluence C7 campaign, with a cumulative D plasma fluence of up to 5×10^{26} m^2 s^{-1} [11], thick deposited layers up to 55 μm were observed [12]. Thick W deposited layers were identified as the likely origin of 'UFOs' observed during that campaign, in around one third of the cases leading to disruptions [11]. In JET dust flaking has also been observed to lead to strong spikes in radiation, which in a small number of cases led to the end of the discharge [13].

The increased W source in ITER may lead to the formation of W layers in deposition regions, particularly in the detached divertor regions as well as shadowed or cold parts of the divertor where ion energies are low such that sputtering is suppressed (although recent work on tungsten entrainment suggests that even here sputtering will be non-zero [14]). These could be of concern as a potential source of dust, which can represent a disruption risk and radiological hazard [15]. For a Be FW and W divertor with scrape-off-layer (SOL) drifts from outer midplane to inner divertor, Romazanov *et al* give a total Be wall source in ITER of around 1.1×10^{23} Be s^{-1}, and a flux to the inner divertor strikepoint of around $\sim 7 \times 10^{20}$ Be m^{-2} s^{-1} [16]. Scaling this value to the W source calculated in [2] gives fluxes in the range $0.03–7 \times 10^{19}$ W m^{-2} s^{-1}, giving an estimated number of 400 s discharges to form micrometer-scale deposits of between 2 and 500.

Conditions in tokamaks vary greatly over the course of an experimental campaign, greatly complicating the analysis of deposited layers which grow and alter over many discharges, particularly in their early stage. At the same time, W films generated in laboratory setups have been extensively studied [17–23], but typically have strongly different (or non-existent) plasma conditions and depositing energies than would be expected in ITER. Film properties are typically a strong and complex function of the depositing particle energy, the surface temperature of the substrate, and the ratio of depositing impurity to ion ratio [24, 25]. This makes it challenging to confidently extrapolate from knowledge of laboratory deposit film properties, such as hardness, density and surface adhesion, to the expected behavior of deposits in ITER. Magnum-PSI experiments were therefore carried out to generate thick W film deposits and to characterize their properties when deposited under high flux plasma conditions. While clearly not a one-to-one representation, the conditions used here would be broadly similar to the fully detached divertor in terms of the low surface temperatures and low electron temperatures and high electron densities [26], though of course a clear difference comes from using a pure Ar plasma.

The majority of flaking events in [11] are correlated to liberation of thick deposited layers from the high-field side of the WEST tokamak during a disruption at the end of the preceding discharge. In ITER the stored energy released during type-I ELMs is comparable to that during disruptions in WEST [27, 28]. This indicates that understanding layer adhesion, and how transient events can affect this, will be critical for ITER. Therefore deposited W layers grown in this study were subsequently subjected to ELM-like loading during plasma to determine how this affected the layer adhesion.

2. Methodology

2.1. Experimental setup

The Magnum-PSI linear plasma device is capable of achieving high-flux plasma loading similar to detached divertor conditions in ITER (high electron density (n_e) and low electron temperature (T_e) with ion fluxes $> 10^{24}$ m^{-2} s^{-1}) [29]. In order to deposit significant W via high flux plasma, a sputter plate setup was used similar to that employed to study the fast growth of tungsten nano-tendrils by Kajita *et al* in [30], as shown in figure 1.

A W sputtering plate ($50 \times 20 \times 2$ mm) was mounted on titanium-zirconium-molybdenum (TZM) mounting rod using

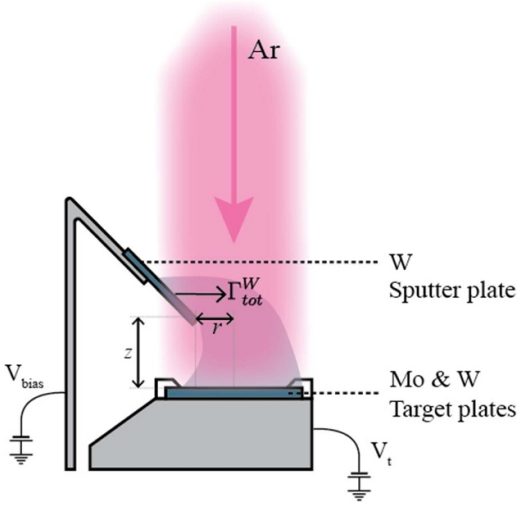

Figure 1. Schematic diagram of the experimental setup used. The Ar plasma impinges on the W sputter plate biased negatively to V_{bias}, resulting in a flux of sputtered W Γ^{w}_{tot} into the plasma, which is then entrained and deposited on the target assembly consisting of W and Mo targets. The position of the W sputter plate can be adjusted in the z and r directions, and the target plates can also be biased to voltage V_{t}.

a Mo screw and attached to the translation arm of the Magnum-PSI multi-target holder using an AlN insulator plate connected via Al_2O_3 bushings enclosing stainless steel screws. This meant that the sputter plate was electrically isolated from the translation arm and multi-target holder and could be biased negatively up to $V_{\text{bias}} = -600\,\text{V}$ defined relative to ground. The sputter plate could be re-positioned relative to the radial r and axial z position of the target assembly center in the range r = 0–24 mm and z = 13.5–45 mm. This plate was exposed to a pure Ar^+ plasma at an angle of 45° with respect to the plasma axis. Ar^+ plasma was chosen to maximize the sputtering rate by the plasma at relatively low V_{bias} as pure D^+ plasmas were found to overheat the sputtering plate at the required V_{bias} to achieve sputtering (the threshold energy for sputtering of W by D is $E_{\text{th}} = 229\,\text{eV}$ [31]), while still presenting conditions of high flux plasma with collision effects between ions and sputtered atoms therefore incorporated. By varying V_{bias} the impacting energy of the Ar ions on the sputter plate $E^{\text{sp}}_{\text{ion}}$ (eV) was varied as

$$\begin{aligned} E^{\text{sp}}_{\text{ion}} &= E_{\text{th}} + E_{\text{sh}} + \Delta E_{\text{bias}} \\ &= 2k_{\text{B}}T_{\text{i}} - \frac{1}{2}k_{\text{B}}T_{\text{e}}\left[\ln\left(\frac{2\pi m_{\text{e}}}{m_{\text{i}}}\right) - 1\right] + e\left(V_{\text{bias}} - V_{\text{f}}\right) \end{aligned} \tag{1}$$

$$E^{\text{sp}}_{\text{ion}} \approx 7.7k_{\text{B}}T_{\text{e}} + e\left(V_{\text{bias}} - V_{\text{f}}\right) \tag{2}$$

where V_{f} is the experimentally measured floating potential of the sputtering plate relative to ground. $T_{\text{e}} = T_{\text{i}}$, $Z_{\text{i}} = 1$, and a pure Ar^+ plasma is assumed.

Because of the relatively high roughness of the as-machined plate, the sputtered W particles are estimated to be sputtered using normal incidence sputtering yields taken from [31], and for the same reason are assumed to erode with a cosine distribution. The sputtered W are also assumed to be sputtered as neutrals with a Thompson energy distribution [32] with average energy taken from [33].

Once the sputtered neutrals enter the plasma they can collide with the plasma and become entrained in the plasma due to ionization and subsequent ion-ion Coulomb collisions or via ion-neutral collision processes [14]. Following the methodology in [14] the entrainment mean free path λ_{ent} can be determined. For the conditions of interest here the range of λ_{ent} is shown in figure 2. These are comparable or smaller than the scale size of the plasma beam in our conditions of interest (section 2.3) such that significant entrainment of W into the Ar plasma can be expected.

The entrained W flux is then deposited on the target assembly, which is shown in figure 3. The target assembly consisted of a cross-shaped set of three W and ten molybdenum (Mo) targets. These were 3 mm thick with surface dimensions 10 × 10 mm and 5 × 10 mm respectively, cut via wire electrical discharge machining. The targets were mounted to the Magnum-PSI multi target holder using a TZM alloy clamping ring secured with six Mo screws. The targets used a 'top hat' geometry to ensure that the surface was flush with the clamping ring, with base dimensions 12 × 10 mm for W and 12 × 5 mm for Mo. The cross shape was chosen to try and maximize the capture of the W deposits and to enable the measurement of weight gain by mass difference measurement (MDM) and evaluation by scanning electron microscopy (SEM) at different localized positions, as described further in section 2.4. W was chosen to have the scientifically most-relevant surface to investigate adhesion and film properties. Mo was chosen firstly because of its similar thermal properties, such that it should reach a similar surface temperature as W, secondly because of its relatively low sputtering yield, such that at floating conditions no sputtering occurs in an Ar plasma (the threshold for sputtering of Mo by Ar is $E_{\text{th}} = 28.6\,\text{eV}$ [31] so no sputtering should occur for $T_{\text{e}} \leqslant 3.7\,\text{eV}$ following equation (2)), and thirdly as a contrast surface where the deposited layer thickness could be resolved using Rutherford backscattering spectroscopy (RBS) as detailed in section 2.4.

Prior to exposure all targets were sandblasted using alumina beads to remove brass cutting traces. All targets except those in set M(R) were subsequently ground using SiC paper and polished via diamond suspension. The goal here was to provide a highly flat surface to enable accurate thickness measurements via RBS, and as contrast to the rough clamping ring. All targets were cleaned using an ultrasonic bath with acetone and ethanol, before finally being outgassed in vacuum for 1 h at 1000 °C. Set M(M) was subsequently sputtered in the Ar^+ plasma by applying a bias to the multi-target-holder of $V_{\text{t}} = -37\,\text{V}$ for 11 s. As a result the gross sputtered thickness for the tungsten targets was around 27 nm, resulting in significant roughening.

Between depositions on different sets the clamping ring was sandblasted using SiO_2 beads and subsequently cleaned using isopropanol between each exposure. This therefore presented a clean and rough surface for each deposition.

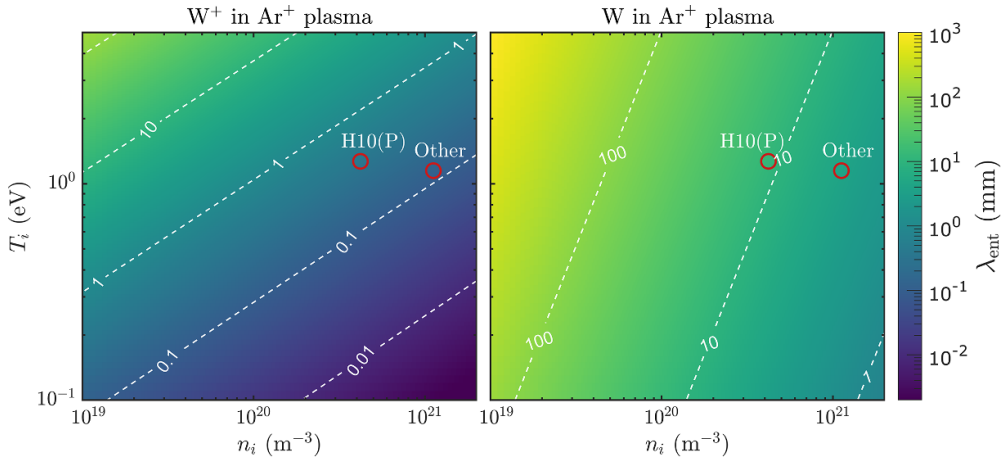

Figure 2. The entrainment length λ_{ent} for W^+ and W impurities in an Ar plasma as a function of the plasma parameters at $r = 0$ (T_i-ion temperature, n_i-ion density). Red circles indicate the experimental conditions corresponding to the target exposures in table 1.

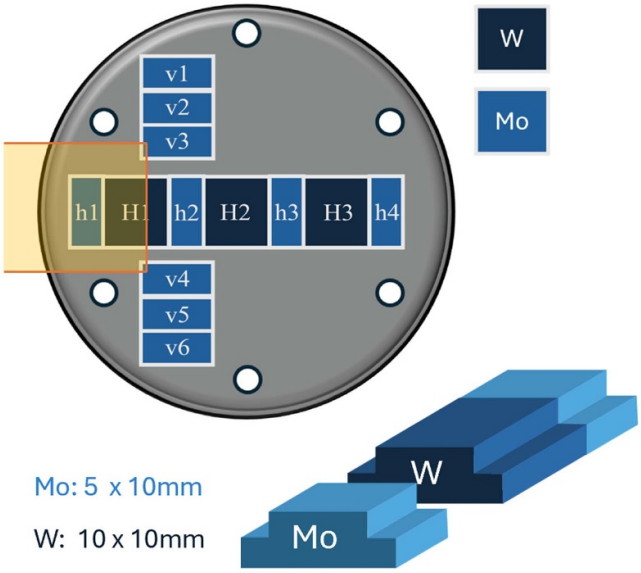

Figure 3. Diagram showing the layout of the target assembly and the labeling convention adopted in this work for each target. The target assembly consist of three W targets with surface dimensions (10×10 mm) and ten Mo targets with surface dimensions (5×10 mm) and had a total diameter of (65 mm). The projected shadow from the sputter target is shown as an orange box for the case where $r = 15$ mm.

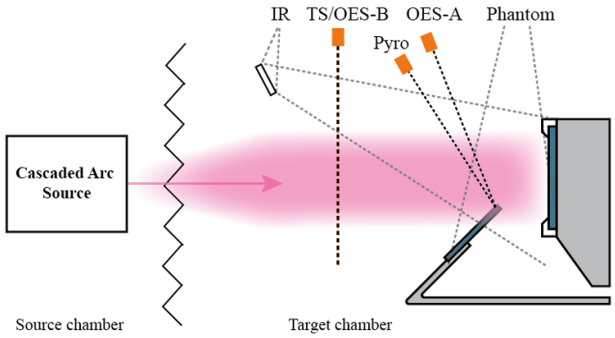

Figure 4. Diagram of the utilized diagnostic setup in Magnum-PSI, showing the position of the Thomson scattering (TS), optical emission survey spectrometer fiber views (OES-A and OES-B), the position of the pyrometer fiber view (pyro) and infra-red (IR) and fast visible (Phantom) cameras.

2.2. Diagnostic setup

An overview of the diagnostic setup in the Magnum-PSI is shown in figure 4. Thomson scattering viewed radially through the plasma at a position 25 mm in front of the sputtering target and was used to determine T_e and n_e profiles as described further in [34]. On-axis peak particle fluxes (Γ_{pk}) and peak heat fluxes (q_{pk}) were determined using the Bohm criterion as described in [35].

Two Avantes survey spectrometers (Avantes ULS2048) were used to monitor the W I 400.8 nm emission line via fiber-optic cable. OES-A was focused on the tip of the sputtering plate and covered the wavelength range 299–451 nm, and OES-B viewed radially through the plasma at the same z position as the TS measurement but azimuthally rotated by 45° and covered the wavelength range 378–476 nm. W I emission was also monitored using a Phantom V12 fast-framing camera viewing tangentially to the target surface through the plasma, and using a 400.8 ± 1.0 nm filter. Due to the use of Ar^+ plasma, Ar I emission lines from the plasma also contributed to the observed signal, but could be subtracted from the observed emission by time filtering.

The temperature of the tip of the sputter plate was monitored using a calibration-free single-chord multi-wavelength pyrometer (FAR-Associates FMPI SpectroPyrometer) with spot diameter of ~5 mm. The end of the sputter plate and the surface temperature of the plate assembly were also monitored using a medium wave infra-red (IR) camera (FLIR SC7500MB, $f = 10 - 6000$ Hz, pixel resolution of ~0.3 mm/px). Two wavelength ranges were covered by use of a filter, either 2.5–5.1 μm without a filter, covering a temperature range 20–450 °C, or 3.97–4.01 μm with a filter

Table 1. Summary of the exposure conditions for each set of targets giving the z position relative to the tip of the sputter plate, the surface roughness prior to biasing the sputter plate (R_s), the ion energy of the Ar^+ ions at the sputter plate surface (E^{sp}_{ion}), the measured current to the plate during biasing (I_{plate}), the sputter yield (Y), the total sputtering flux from the plate (Γ^W_{tot}), the bias duration (t_{bias}) and the total sputtering fluence from the plate (ϕ^w_{tot}).

Set label	z (mm)	R_s (μm)	E^{sp}_{ion} (eV)	I_{plate} (A)	Y	Γ^W_{tot} (atoms s^{-1})	t_{bias} (s)	ϕ^w_{tot} (atoms)
L(P)	20	<0.1	72	1.13	0.01	7.1×10^{16}	5600	3.9×10^{20}
M(P)	20	<0.1	111	1.25	0.07	5.4×10^{17}	1000	5.4×10^{20}
H(P)	20	<0.1	262	0.95	0.35	2.1×10^{18}	170	3.5×10^{20}
M(M)	20	0.1–0.2	111	1.05	0.07	4.6×10^{17}	1000	4.6×10^{20}
M(R)	20	~1.0	111	1.35	0.07	5.9×10^{17}	1000	5.9×10^{20}
H10(P)	20	<0.1	111	3.55	0.07	1.5×10^{18}	2600	4.0×10^{21}
Mz40(P)	40	<0.1	111	1.84	0.07	8.0×10^{17}	1000	8.0×10^{20}

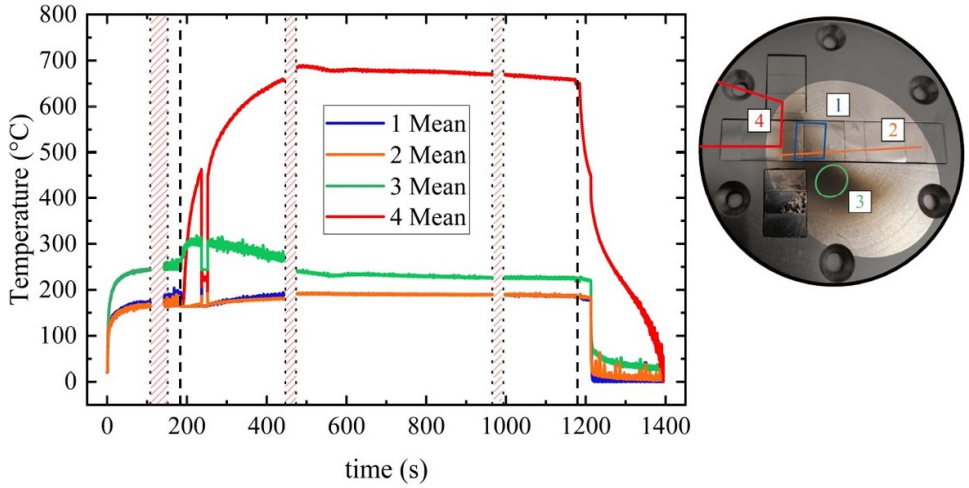

Figure 5. Time evolution of the mean temperature of different surface regions, as indicated on the right hand side, during exposure M(P). Red hashed regions indicate moments where the IR camera filter was switched. The bias is switched on at ~180 s and turned off at ~1170 s, marked by the black dashed lines, as seen in the heating and cooling of the sputter plate (region 4), which is much hotter than the other regions. An emissivity of $\varepsilon = 0.1$ was assumed for all surfaces.

with a 60% transmission covering a temperature range from ~200–1000 °C.

2.3. Deposition conditions

The exposure conditions and resultant sputter rates of the W plate are shown in table 1. All target sets were exposed to an Ar^+ in Magnum-PSI with the sputter plate at $r \approx 15$ mm except for set Mz40(P) where $r \approx 13$ mm . Each discharge ran for a pre-bias time of $t_{pre} \approx 180$ s in order for the target surfaces to reach thermal equilibrium at a temperature between 200 and 300 °C (figure 5). Bias to the sputter plate was then applied at V_{bias} for time t_{bias}, before the discharge continued for a post-biasing time of $t_{post} \approx 30$ s before the discharge ended. From the Thomson Scattering measurements the plasma had a Gaussian profile with a Full Width Half Maximum of $w = 30.0$ mm, and with peak electron temperature $T_e = 1.15$ eV and electron density $n_e = 11.2 \times 10^{20}$ m^{-3}, except for set H10(P). The general aim was to produce similar total fluences of sputtered tungsten from the sputter plate (generally ϕ^w_{tot} in the range 4–6$\times 10^{20}$ atoms) by adjusting the plasma duration to compensate for a lower sputtering yield, depending on the bias applied. Target set H10(P) was exposed to a significantly wider plasma ($w = 44.5$ mm, $T_e = 1.27$ eV, $n_e = 4.2 \times 10^{20}$ m^{-3}), and for a longer duration than others at the medium bias voltage, and as a result ϕ^w_{tot} was around ten times higher than the other targets, creating extra-thick deposition layers.

The parameters of interest were varied as follows, creating several sets of data:

- The sputter, and thus deposition, rate was varied by changing the value of E^{sp}_{ion} at constant exposure conditions, and depositing on target sets that were polished resulting in set L(P), M(P) and H(P).
- The surface roughness R_s was varied while exposure conditions and E^{sp}_{ion} were held constant, resulting in set M(P), M(M) and M(R).
- The deposition time t_{bias} at high sputter rate Γ^W_{tot} was varied to change the total sputter fluence ϕ^w_{tot} by a factor of 10 to create thicker or thinner layers at the same deposition rate, resulting in set H(P) and H10(P).
- The z position of the sputter plate was varied from $z = 20$ mm to $z = 40$ mm at constant plasma conditions and E^{sp}_{ion}, thus varying the path length and relative energy of the sputtered W due to collisions with the plasma, resulting in

set M(P) and Mz40(P). Due to the z adjustment of the plate r also varied slightly, such that $\Gamma^{W}_{\mathrm{tot}}$ was slightly higher for Mz40(P) than M(P). However ϕ^{w}_{tot} is still within 50%, meaning the results are generally comparable.

2.4. Post-exposure analysis

Deposition thickness was evaluated via three complementary methods:

(1) MDM: here each target was weighed before and after exposure to get the average mass gain over the surface using a Metler Toledo NewClassic MF MS105DU scale, accurate to $\pm 10\,\mu$g. The thickness of the layer was estimated assuming the density of bulk tungsten ($\rho_W = 19250\,\mathrm{kg\,m^{-3}}$).
(2) RBS: this analysis was applied to Mo targets and to the clamping ring, as this requires a lighter substrate material in order to distinguish the heavier deposited W. A standalone ion beam analysis station (IBAS) at DIFFER is connected to a 3.5 MeV singletron ion accelerator manufactured by High Voltage Engineering Europa B.V. This was used to direct H^+ ions in the energy range 2.1–2.3 MeV onto measurement spots of $1 \times 1\,\mathrm{mm^2}$ enabling Mo layer thicknesses up to $\sim 8\,\mu$m to be determined in this localized region. The scattering angle between incident beam and detector was $\theta = 170°$. The beam energy was calibrated using silicon, chromium, silver, zinc and platinum coated silicon samples. The recorded spectra were analyzed using the SimNRA [36] and IBA DataFurnace (NDF) [37] codes. The thickness determination assumes bulk density of the elements identified in the proportions they are detected in.
(3) FIB-SEM: cross sections through the surface were made on selected targets using a focused ion beam (FIB) of Ga^+ ions accelerated to 30 keV. These were then imaged via SEM using a Zeiss CrossBeam 540. A platinum capping layer was added prior to the FIB cross section to protect the surface from damage.

Additional SEM was also carried out using a Thermo Fischer Pharos to image the surfaces of targets. Energy dispersive x-ray spectroscopy (EDX) was used in both SEM devices to estimate the mass concentration at the surface and as a function of depth on the cross-section (FIB-SEM) images.

Nuclear reaction analysis (NRA) was used to evaluate the content of oxygen in the deposited layers using the reaction $^{16}\mathrm{O}(^3\mathrm{He}, \mathrm{p0} - \mathrm{p3})^{18}\mathrm{F}$ using the IBAS setup described above. This used an ion energy of 2.3 MeV with an angle of $\theta = 170°$. A 19.5 μm Kapton foil was used in front of the NRA detector to remove the RBS signal, and a calibration was carried out using a 275 nm a-C:D sample with known deuterium concentration.

X-ray diffraction (XRD) measurements were carried out on selected targets using a Bruker D8-eco Cu Ka x-ray diffractometer with a $\leqslant 0.02°(2\theta)$ accuracy in diffraction peak position. Approximately 85% of the x-ray signal is estimated to originate from the upper 1 μm. The results were used to determine the crystallite sizes of the layers using the Scherrer formula [38]. Further XRD structural analysis was carried out using a Rigaku SmartLab XE x-ray Diffractometer with 2θ resolution of 0.006° FWHM. Grazing Incidence XRD was adopted setting $\omega = 1°$ to isolate the signal from the surface layer of the film (about 100 nm). This was used for detailed surface mapping of the crystallinity of the deposited layers, as well as the phase of the W deposition.

Nano-hardness of the deposited layer was measured using nano-indentation on selected targets with at least several hundred nm layer thickness of deposition. An MTS NanoIndenter XP with a TB11291 diamond Berkovich tip was used with a maximum load of 3 mN. This load was chosen such that indents would be of the order 100–200 nm in order to stay below 10% of the total film thickness to avoid unwanted substrate influence. On each sample 25 separate indentations were made in a 5×5 grid of 0.5×0.5 mm on regions which were relatively flat, without flaking, cracking or other defects to ensure good quality. These were filtered for abnormal load-displacement curves which were excluded from the subsequent averaging. Hardness was determined using the Oliver-Pharr method [39, 40].

Scratch testing was carried out to study layer adhesion using a MCTX S/N 50-0223 (CSM instruments) equipped with a Rockwell indenter and a 200 μm spherical diamond tip. A linearly increasing load from 0.03 N to 30 N was applied over a scratch length of 3 mm (constant speed of 1 mm $\mathrm{min^{-1}}$). Morphological analysis of the scratch marks was performed using a high-resolution Field-Emission SEM Zeiss Supra 40 equipped with a Gemini column and coupled with an Oxford Instrument EDX spectrometer. The accelerating voltage was 5 kV.

2.5. ELM-like loading

Selected targets were subjected to subsequent deuterium plasma loading in Magnum-PSI, in combination with simultaneous ELM-like loading using a 1064 nm Nd:YAG laser (LASAG FLS 352–302). The plasma settings were chosen such that the surface temperature of each sample was set to be 700 °C, with $T_e = 1.06 \pm 0.03$ eV and $n_e = 6.8 \pm 0.6\,\mathrm{m^{-3}}$. Two sets of ELM-like loading were carried out, and the location was visually inspected between the two sets of loading. In each case a pulse duration $t = 1$ ms was used with first heat flux factor ($F_{\mathrm{HF}} = 6\,\mathrm{MW\,m^{-2}\,s^{0.5}}$ and pulse number $N_{\mathrm{pulse}} = 10^3$ and second $F_{\mathrm{HF}} = 9\,\mathrm{MW\,m^{-2}\,s^{0.5}}$ and pulse number $N_{\mathrm{pulse}} = 10^4$). The laser spot was Gaussian with a FWHM of $\sim$5 mm. These settings were chosen to enable comparison with known damage under similar loading from Morgan *et al* [41], which for bulk tungsten result in either surface roughening or crack network formation respectively [42].

3. Results and discussion

3.1. W entrainment

As shown in figure 2 the entrainment path lengths λ_{ent} are short in the plasma compared to the FWHM w. The exact path

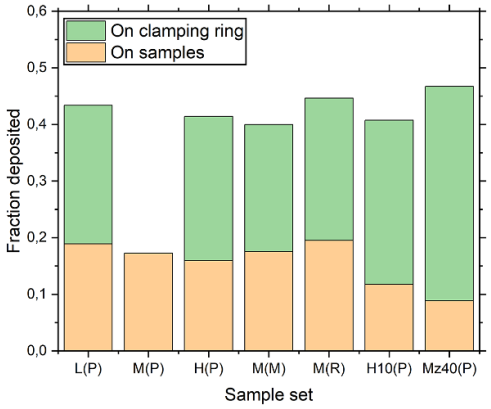

Figure 6. Summary of the fraction of tungsten deposited on the sample set and clamping rings, and the total fraction, relative to ϕ^{w}_{tot}. No data was available for the deposition fraction on the clamping ring for sample M(P).

lengths, angular sputtering distribution and velocity distribution are uncertain, but we should expect a significant fraction of the sputtered tungsten to be entrained in the plasma. Based on the solid angle with respect to the target and assuming the worst case scenario for azimuthal distribution, i.e. a uniform angular distribution over 2π, would suggest that for the experiments done with $z = 20$ mm the line-of-sight captured fraction should be $\sim$10% and for $z = 40$ mm only $\sim$3%. Based on MDM the total amount for each sample set (except set M(P) where this was not possible) is quite similar, with values in the range 40%–47%, as shown in figure 6. The fact that the $z = 40$ mm and $z = 20$ mm values are similar is also strong evidence of the entrainment effect. The entrainment fraction for a sputtered particle with a trajectory towards the plasma center from the edge of the sputter plate can be estimated as [43]

$$f_{\mathrm{ent}} \approx 1 - \exp\left(-\frac{r + w/2}{\lambda_{\mathrm{ent}}}\right) \tag{3}$$

For all cases this gives $f_{\mathrm{ent}} \approx 1$, while on the other hand the particles which have trajectories away from the plasma center would have $f_{\mathrm{ent}} \to 0$. meaning for a uniform angular distribution around 50% of the particles would be captured, broadly in line with these observations.

An additional effect of the entrainment is an increased energy of the deposited W ions. Following the methodology in [14] the ion impact energy for W^+ would be $E_{\mathrm{i}} \approx 10 k_{\mathrm{B}} T_{\mathrm{e}}$ for full entrainment at the sheath entrance compared to $E_{\mathrm{i}} \approx 5 k_{\mathrm{B}} T_{\mathrm{e}}$ with zero entrainment. Higher ion energies result in increased mobility of the deposited atoms and longer transport, typically resulting in larger grains with fewer defects, mimicking the effect of having a higher temperature substrate [44]. It should be noted that given the long connection length from the FW region to the divertor the W ions in the SOL of ITER would be likely to become fully entrained, at least in the higher density regions close to the separatrix, and that full entrainment would result in an ion energy at the wall for W^+ of $E_{\mathrm{i}} \approx 78 k_{\mathrm{B}} T_{\mathrm{e}}$ for a DT plasma due to the much greater mass difference between W and D or T.

The entrainment can also be seen in figure 7. The Phantom camera images (figure 7(*a*) and 7(*b*)) show the W I emission in the region close to the target. The bright light from the sputter plate shows contributions from neutral W excitation but also close-lying Ar emission lines, as well as grey-body emission from the sputter plate, which is sufficiently hot (1190 ± 10°C) to emit in the visible spectrum. On the other hand the non-symmetric emission at the lower side of the target can be attributed to W I emission. The asymmetry arises from $\mathbf{E} \times \mathbf{B}$ rotation in the plasma (anti-clockwise as viewed from source to target) due to the radial electric field of Magnum-PSI [45, 46]. The entrained W follows this rotation, resulting in emission being shifted towards the bottom of the image (figures 7(*a*) and (*b*)). This can also be seen in the observed deposition pattern on the target, as shown in examples in figures 7(*c*) and (*d*). The longer path length from the sputter plate to the target for set Mz40(P) leads to the light being shifted further down (figure 7(*b*)) and correspondingly the deposition pattern is more spread out and rotated further (figure 7(*d*)). This is confirmed from MDM of the targets and the clamping ring, which show that the fraction of deposited W material on the targets sets compared to the total on target sets plus clamping ring was 16.7 ± 4.6% for the samples with $z = 20$ mm while for the set Mz40(P) with $z = 40$ mm this was only 8.9%.

3.2. Layer thickness and properties

From the MDM and RBS measurements the thickness of the deposited layers could be determined. Two examples of the distribution of average thickness on each target and the average on the clamping ring are shown in figures 7(*e*) and (*f*). Comparing just these two cases, this shows that the thicknesses vary dramatically across the surface from only a few 100 nm on Mz40(P)v1 to above 10 μm on M(R)H2. Layer thicknesses above 50 μm were measured on target H10(P)v6, as this experiment had the highest value of ϕ^{w}_{tot}. The most detailed deposition profile can be determined from RBS measurements of the final experiment (M(M)) where also RBS of the deposition profile on the clamping ring could be acquired, combined with available RBS data from set M(P). This is shown in figure 8.

In order to constrain the RBS fitting process, it is necessary to know something about the composition and density of the deposited layers. FIB cross sections of selected layers are shown in figures 9(*a*) and (*b*). These figures show that the layers are highly compact with a mixed grain structure with a more fine crystalline close to the target surface transitioning to a columnar grain structure towards the outer surface. This is in line with other tungsten coatings produced with Magnetron sputtering [17–20] and PLD [20, 21, 47], and suggests transition zone (Zone T) growth when placed onto the structural zone model of Thornton [24]. Such grain structures occur at low pressures for surface temperatures relative to the melting temperature of $T/T_m \leqslant 0.5$, which is in line with the temperatures observed here ($T/T_m \leqslant \sim 0.15$), as shown in figure 5.

The FIB images also show the formation of nodular growth flaws. These were observed to be much more common on rough than polished substrates (contrast figures 9(*a*) and (*b*)).

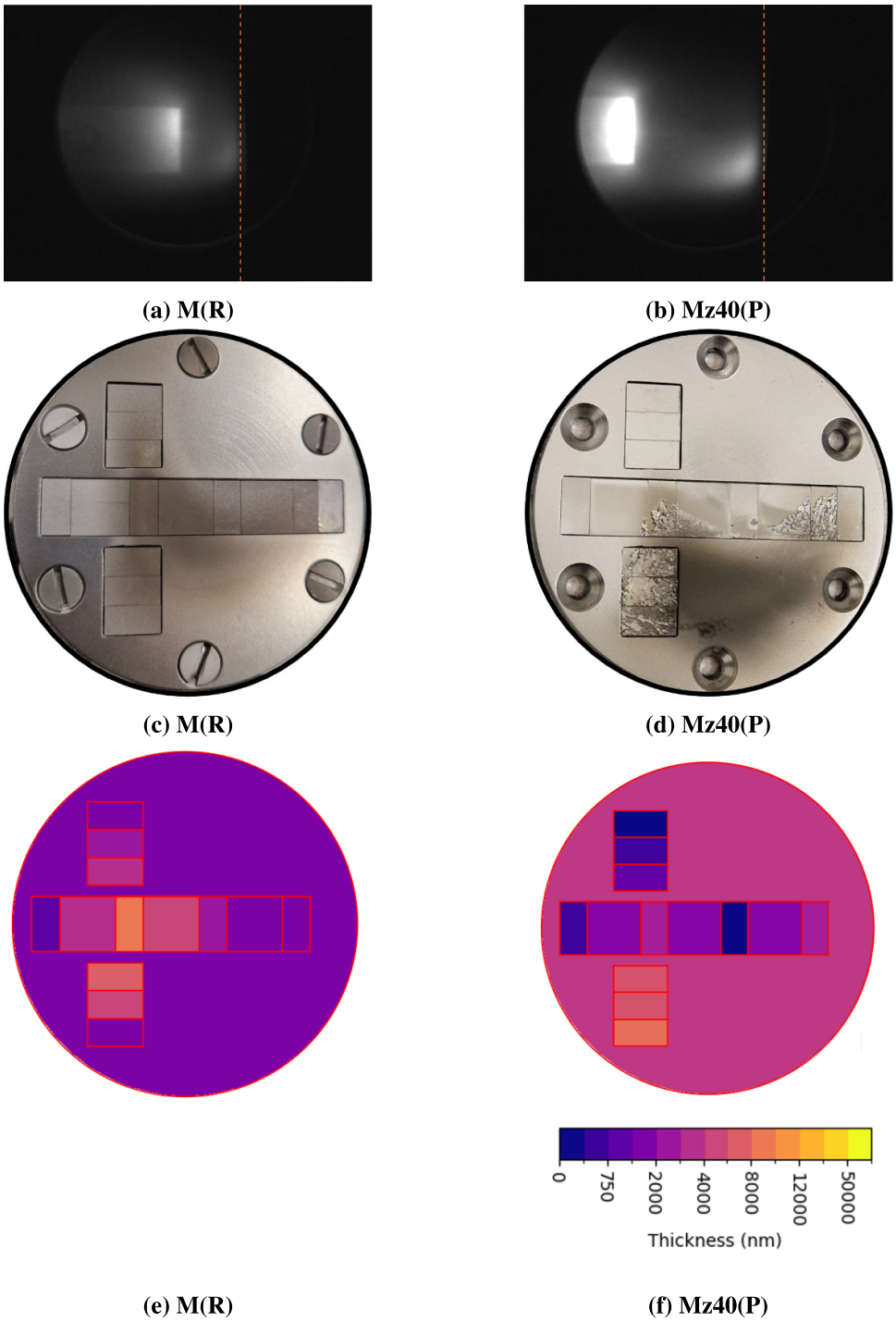

Figure 7. Above: filtered Phantom camera images of the W 400.8 nm light emission from the plasma for (*a*) set M(R) and (*b*) set Mz40(P). The orange dashed line indicates the target assembly surface. Middle: post-exposure deposition patterns for (*c*) set M(R) and (*d*) set Mz40(P). Below: average deposition layer thicknesses from MDM for (*e*) set M(R) and (*f*) set Mz40(P).

Such growth flaws typically result from preferential nucleation and growth at debris particles or other surface irregularities [24], therefore the formation of more of these on rough samples is consistent. These growth flaws likely play a role in adhesion as discussed further in section 3.3.

EDX analysis was performed on selected FIB cross sections, and a typical example is shown in figure 10(*a*). For samples on Mo substrates a small Mo concentration is found around 10 wt.% close to the substrate which decreases to around 5 wt.% at the deposit surface. EDX of W substrates do not show any Mo presence which indicates that the Mo originates most likely from the substrate itself. A possible source is from the FIB cutting process, where small amounts of the Mo are deposited onto the layer surface, despite the use of a protective Pt layer. However, the RBS fitting process also show that addition of at least one additional element consistently

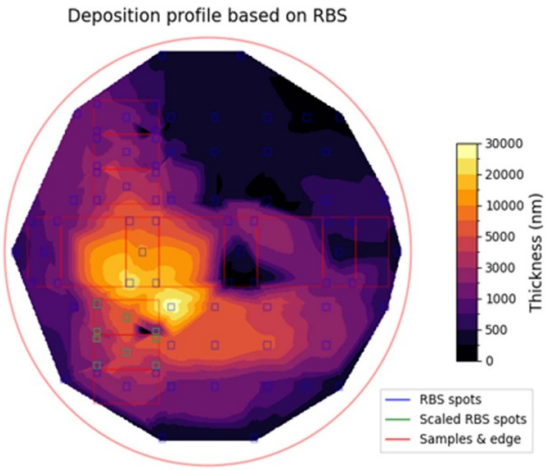

Figure 8. Detailed mapping with RBS of the deposited layer thickness for target M(P) and clamping ring M(M). These are combined to one map as the loading conditions were nearly identical by scaling the clamping ring values by the ratio $f = \phi^{w}_{\mathrm{tot,M(P)}} / \phi^{w}_{\mathrm{tot,M(M)}}$. The points are interpolated to create a thickness color map. The scaled data points in green are from target set M(M) to M(R) by the same scaling factor f due to flaking making the RBS data unrepresentative of the total deposited thickness.

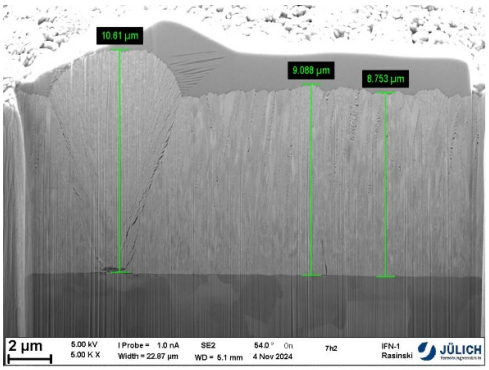

(a) M(P)h2

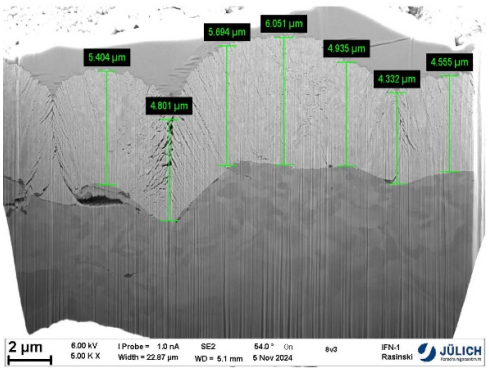

(b) M(R)v3

Figure 9. FIB cross section images of (*a*) target M(P)h2 (*b*) target M(R)v3. Green vertical lines indicate the measured deposit thickness in the black boxes inset in the images.

gives a superior fit compared to assuming a pure W layer. The EDX analysis rules out other higher-Z elements, but EDX is less sensitive for low-Z elements. Low-Z elements such as H,

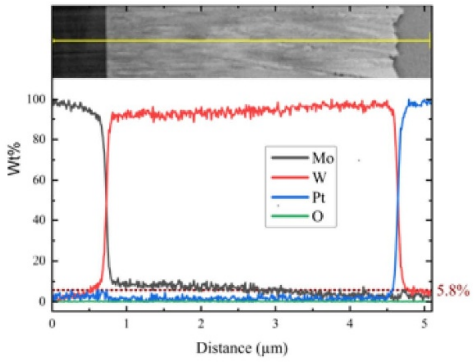

(a) M(P)v3

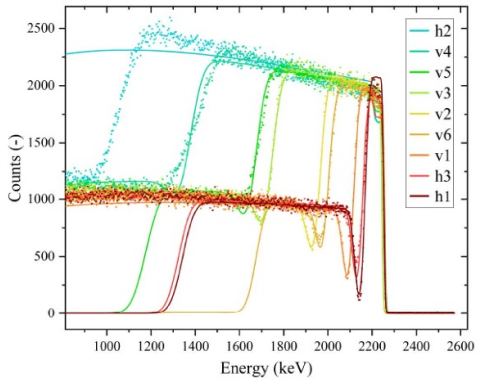

(b) M(M)

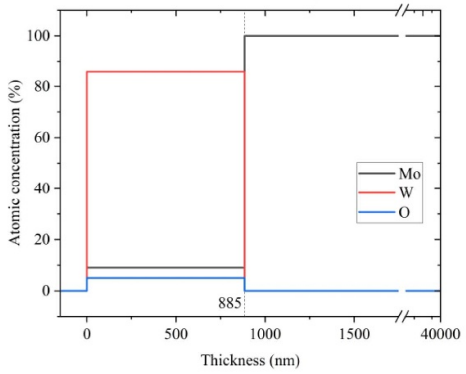

(c) M(M)v1

Figure 10. (*a*) The EDX wt.% depth profile of target M(P)v3. (*b*) the RBS fits for the Mo targets of exposure M(M). (*c*) the RBS depth profile resulting from the fitting for target M(M)v1.

He, Li and B would be undetectable via EDX but no source is present that could produce a significant contribution to the deposition layer from these elements. A possible second element could be oxygen. NRA analysis of target M(P)v3 was carried out and compared to a reference SiO_2 sample of known thickness (1.5 μm). By comparing the oxygen peaks of both samples while using the known layer thickness we can estimate that the oxygen content of the layers is below 5%. This is consistent with the EDX results which shows an oxygen wt.% of below 1% ($<$ 4.8 at.%). A constant 12 at.% Mo concentration and an O 5 at.% concentration with the balance W

gave the best RBS fits for all measurements (figure 10(*b*)), resulting in uniform composition profiles as a function of depth (figure 10(*c*)). This is therefore taken into account in determining the effective thickness of W deposition at each measured position as shown in figure 8. The question of whether or not a small fraction of the deposit is Mo is however unresolved. Another possible source of Mo is from the TZM support rod for the sputtering plate, which was also biased, however no Mo lines were observed via OES-B. Given the disagreement between EDX cross-section and RBS results, it is not possible to draw a clear conclusion.

Additional properties of the layers were also investigated. The hardness of selected layers was evaluated using nano-indentation, and the results are shown in figure 11(*a*). This shows that the hardness values vary widely but are typically much higher than that for bulk tungsten, while being comparable to other thin film layers. Typically Zone T structures have a high hardness due to a high dislocation density as well as the Hall–Petch relationship due to their small grain structure [24]. At high thicknesses there is much sparser data, but there is some indication for a reduction in hardness back towards the bulk properties, which can be related to the transitional microstructure for Zone T deposits seen here as the larger grain sizes at the surface of these layers will lead to lower hardness due to the Hall–Petch relationship.

Crystallite domain size was measured via XRD and compared to literature values as shown in figure 11(*b*). This shows a wide spread of values with, again, comparable values to literature. Examination of the XRD 2θ distribution show a polycrystalline rather than amorphous structure, which agrees with the FIB and SEM observations. Crystallite sizes are mostly smaller than measured bulk reference materials, as is typical for thin films. There is no clear relationship between domain size and layer thickness, as might be expected [50], indicating that other factors play a role here. Sala *et al* [49] showed that α-W forms small crystallite sizes that grow after annealing from around 15 nm up to 90 nm, with the transition starting around 500 °C. Given that the deposition temperatures were much lower here the substrate temperature should not be playing a strong role in crystallite size either. From peak positions, predominantly the coatings are α-W, though small regions of β-W are seen in some locations, for example in H(P)H3 (figure 11(*c*)). This region is a region with one of the highest deposition rates of those examined, suggesting that the meta-stable β-W phase may form when the high rate of arriving species limits their surface diffusion and prevents migration into the stable α-W phase. Of the investigated targets, the other of interest is L(P)H3, which shows some additional non-W peaks. These are tentatively attributed to Al, based on the analysis of peaks at 37.57°, 43.39°, 63.48°, 75.50° and 80.31°, which agree with an FCC structure with lattice parameter 4.15 Å , which is somewhat close to that of Al (4.05 Å). EDX mapping shows Al-rich residue in this region, which may originate from the alumina-bead sandblasting carried out during the sample preparation.

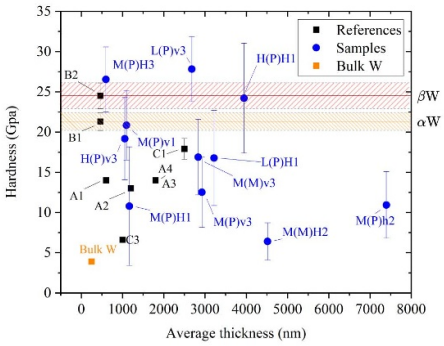

(a) Thickness vs Hardness

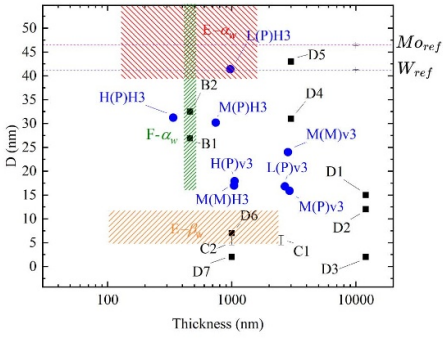

(b) Thickness vs Crystallite size

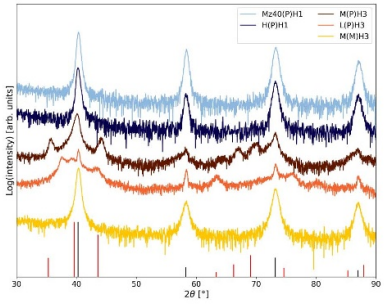

(c) XRD spectra

Figure 11. (*a*) Deposited layer thickness vs hardness for selected targets compared to bulk tungsten [48] and references A [18], B [17] and C [22]. The average hardness values for α-W and β-W are taken from [17, 23]. (*b*) Deposited layer thickness vs crystallite domain size for selected targets measured by XRD. Measured Mo and W reference surfaces are also shown. Literature values from B [17], C [22] and D [20], as well as measured values of α-W and β-W from E [23] and of α-W from F [49] are also shown. (*c*) XRD spectra of selected targets. The black and red lines indicate the angular peak positions for α-W and β-W respectively.

3.3. Adhesion of layers

In the course of the experiments significant flaking and delamination is observed. This can be seen in figures 7(*c*) and (*d*) for example. From IR camera recordings it can be seen that this occurs dynamically during the deposition process (figure 12) where the bright regions which increase over time are poorly adhered regions which are therefore poorly cooled

Figure 12. IR camera stills from the exposure of target set M(P). The blue dotted lines outline the position of the W sputtering plate, which is heated and therefore glows. The orange dotted lines indicate the positions of different targets in the clamping ring assembly. The bright regions increase in size over time, and are indicative of poorly adhered layers which are then badly cooled and thus strongly heated by the plasma. At 199 s the bright regions have disappeared, showing that these regions have flaked from the surface.

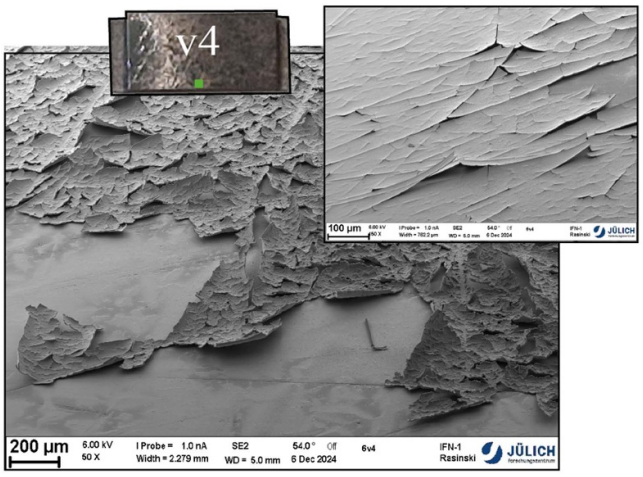

Figure 13. Example SEM images of deposition on a polished target H(P)v4 showing typical flaking behavior. The location of the two images is indicated by a green square on the inset photograph.

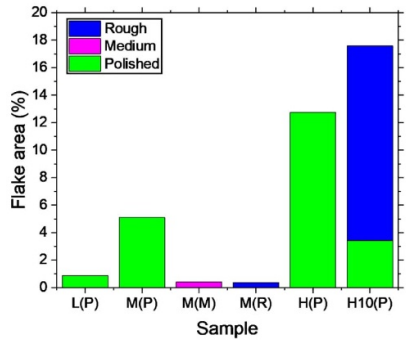

(a) Surface roughness vs flake area

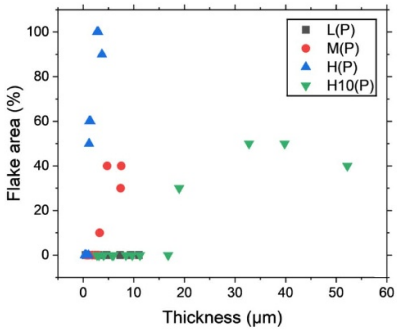

(b) Thickness vs flake area

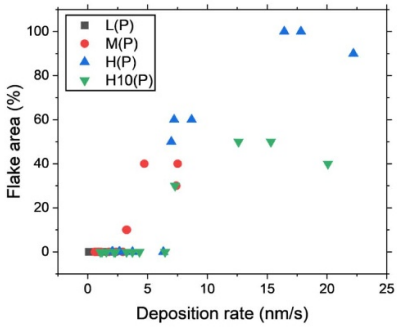

(c) Deposition rate vs flake area

Figure 14. Correlation between (*a*) flaked area of the assembly targets and clamping ring compared to the total surface area of those surfaces, indicating also the roughness of the different surfaces (clamping ring is always rough). (*b*) total average thickness of each target and (*c*) local average deposition rate compared to the flake area of each target for sets L(P), M(P), H(P) and H10(P).

and hot. This indicates that in some cases the build-up of the tungsten layer leads to strong residual stresses which lead to a delamination of the surface in certain regions. This can be seen in the surfaces shown in figure 13 which show upwardly curled peeling and delamination of the surface, which is characteristic of strong tensile stresses. These flaking regions grow over time, suggesting a threshold for flaking to occur, rather than happening due to e.g. cooling at the end of the discharge or due to exposure to atmosphere. The flaking appears to predominantly initiate at corners, scratches or other discontinuities in the deposited layer (e.g. 13, inset).

Such thresholds can be linked to various parameters and properties. Correlating surface flaking coverage defined from post-mortem photographs to substrate parameters and deposition rate and thickness enables evaluation of which factors play a leading role. These are shown in figure 14. These indicate that firstly, high surface roughness strongly reduces the amount of flaking occurring, which can be most clearly observed comparing sets M(P), M(M) and M(R) in

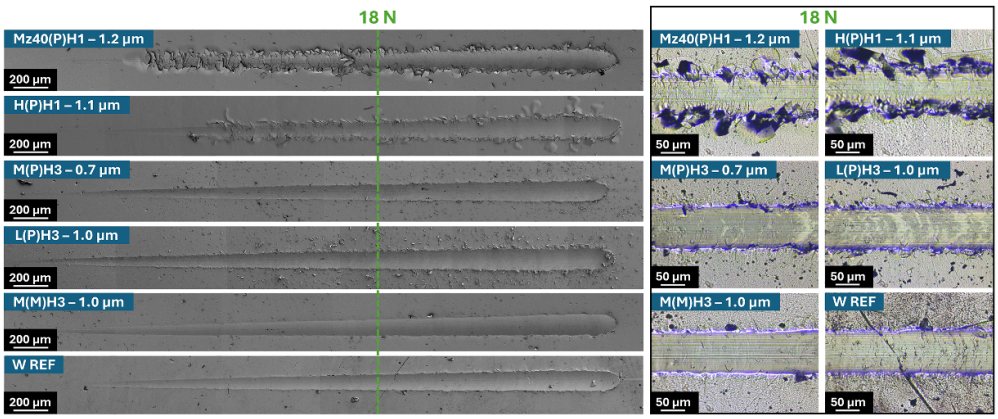

Figure 15. SEM figures giving a summary of scratch testing results showing deposited layers in increasing adhesion order, with the sample and estimated thickness, based on MDM, indicated above the stitched SEM images. A tungsten reference sample without coating is also shown for comparison. A magnified image of the region loaded at 18 N (indicated by the green dashed line on the stitched SEM images) is shown on the right.

figure 14(*a*). This can be understood from the reduction in residual stresses on rough surfaces due to the high concentration of nodular growth flaws on rough substrates as seen in figure 9. Nonetheless figure 14(*a*) does show that flaking from rough surfaces did occur on some regions, particularly for set H10(P) where a large region of flaking on the rough clamping ring was observed. Average thickness from MDM of the clamping ring was around 3 μm, but locally would have been much thicker. From RBS measurements of the clamping ring after exposure M(P) the factor between maximum and average thickness was around a factor 30 (figure 8), so that these regions could have been approximately $\sim$90 μm thick, but were likely thinner than this. This suggests that a sufficient thickness may average out the initial surface roughness to make flaking more likely by reducing nodal growth, or that sufficiently thick layers may have an increasing probability of flaking. This is corroborated by figure 14(*b*) which shows that for polished substrates all layers thicker than 19 μm had at least some surface flaking. On the other hand, much greater amounts of flaking are observed for much thinner total layer thicknesses in some cases. This can be better understood by examining figure 14(*c*), which shows a clearer positive correlation between flaking and deposition rate.

Overall the tensile stresses that arise can be understood from the model of Hoffman [51], which posits that interfacial energy decrease is a driving force to form grain boundaries which gives rise to a tensile stress in the material. In the model of Chason *et al* [52] this mechanism is used to derive the tensile stresses arising in the material σ_T as

$$\sigma_T \propto \sigma_{T0} \exp\left(-\frac{D}{RL}\right) \tag{4}$$

where D is the effective diffusivity of atoms to move from the surface to the triple junction of the grain boundary, R is the deposition rate and L the grain size. For small values of D/RL, i.e. low diffusivity, high deposition rate or large grain size, the tensile stress will be large. The dependence on thickness and on growth rate can therefore be understood as, due to the Zone T growth, grain size increased with thickness as seen in figure 9. Layers sufficiently thick, or with a fast enough growth rate, should be under the largest tensile stresses and therefore most vulnerable to flaking, in line with observations of Engwall *et al* [53].

This is corroborated by scratch testing carried out on selected targets which all had layer thicknesses around 1 μm, which are summarized in figure 15. The scratch testing indicates a variety of adhesion types on different surfaces. For example, sample H(P)H1 shows clear buckling failure at higher stylus loads above 18 N, which is a characteristic failure mode for hard coatings below 10 μm thickness [54]. Additionally edge chipping is seen, where the coating lifts and fractures outside of the scratch track. On the other hand sample M(M)H3 shows no buckling, chipping or other types of delamination, and in fact is quite similar to a bulk W sample also shown at the bottom. Well adhered samples do show clear delamination, but with cracking over only a small region at the edge of the scratch trace. The observed ordering is generally in line with the results from the flaking correlations, with an increasing adhesion with lower deposition rate, and better adhesion also seen on the rougher substrate. An additional factor appears to also be whether the samples were directly exposed to plasma or shadowed by the sputter plate. The H1 targets were shadowed, so W arriving there had to be transported by diffusion or rotational transport from the plasma column, while W at the H3 targets were closer to the center of the plasma and were not shadowed. The H1 targets both had significantly worse adhesion than the H3 targets, as only the H1 targets showed edge chipping, indicating that the plasma played a role in the adhesion, possibly by improving the initial adhesion on the surface, for example by plasma cleaning, or that adhesion was improved due to the higher ion energies at the plasma center where entrainment would be more complete. Alternatively the fact that the H1 targets were shadowed may mean they were colder and therefore less

Table 2. Summary of the targets exposed under ELM-like loading and their behavior. Labels in the final three columns indicate Yes (Y), No (N) or unclear (?).

Target label	W Layer thickness (nm)	Flaking	Melt areas	Bulk cracking
M(P)H1	750	N	N	Y
H(P)H2	1450	Y	Y	Y
M(P)H2	3270	Y	N	N
M(P)v4	7520	Y	Y	?
M(R)H1	750	N	N	?
M(R)H2	5720	N	N	?
M(R)v4	7880	N	N	N

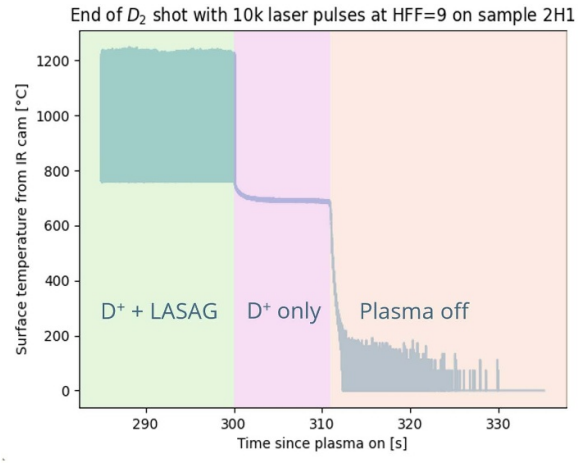

Figure 16. Example time-trace of the surface temperature of the center of the laser loaded region of target M(P)H1 at the end of the discharge, with $N_{\mathrm{pulse}} = 10^4$ and $F_{\mathrm{HF}} = 9\,\mathrm{MW\,m^{-2}\,s^{0.5}}$.

likely to be well adhered. On sample H(P)H1 regions of compressive stresses (indicated by clear buckling over a region of a few mm in diameter) were observed far into the shadowed region, rather than tensile stress regions, which on the other hand were observable in the region closer to the plasma center.

3.4. ELM-like loading adhesion testing

Simultaneous deuterium plasma and ELM-like loading was carried out on selected targets from the prior round of W deposition described above. The results of the loading are summarized in table 2. An example of a typical time trace recorded by the IR camera is shown in figure 16. From the first of the two rounds of loading, no clear visual changes were observed. This first round used low values for F_{HF} and N_{pulse} to screen for very limited adhesion, as for bulk tungsten only surface roughening and light plasma surface etching was previously observed [41]. The fact that no changes were seen implies that all layers were at least somewhat adhered to the surface. The second round of loading used much more intense loading conditions which should be expected to create a crack network. This was indeed found on all samples, but two different types of behavior were observed. SEM images of the two main types of behavior are shown in figures 17(*a*) and (*b*). Of the selected targets, only those with a polished surface showed clear flaking behavior at the laser-loaded region. For the thinnest two layers on these polished substrates, the crack network also clearly extended into the bulk. This suggests that here there was still good adhesion to the surface so that heat was able to flow into the bulk and thermally stress the material enough for it to crack. On the other hand for two of the three cases where flaking was observed, material at the edge of the flaked areas were observed to melt into small blobs (figure 17(*c*)). These indicate small regions where no adhesion to the surface still exists, resulting in heating far above the surface average leading to melting. For the rough surfaces, a crack network also forms, however no flaking is observed, and no poorly adhered regions with melted blobs are observed. This is consistent with the better adhesion found in section 3.3 for rough samples. In most cases no cracking extending to the bulk can be definitively identified as the cracks are not wide enough to see the bulk. In the case of M(R)v4 the cracks are large and no cracking can be seen underneath. This does suggest that most of the heat goes into decohesion of the deposition layer, which may eventually lead to flaking, but no clear evidence for this can be observed.

3.5. Conclusions and implications for ITER

In this study we have successfully demonstrated the growth of thick deposited tungsten layers by physical sputtering and subsequent entrainment of a tungsten sputter plate in an Ar^+ plasma using the Magnum-PSI linear plasma device. The entrainment and thermalization of W species in the plasma may be more representative of expected conditions in the SOL of ITER, which can help to predict the formation and properties of the deposited layers. Evident tungsten entrainment was identified from the high and consistent capture fraction of W on the targets and clamping ring at fractions much higher (40%–47%) than would be expected from line-of-sight deposition (3%–10%). A crescent shaped deposition pattern was observed on the target assemblies due to $\mathbf{E} \times \mathbf{B}$ rotation of the plasma. Grown W layers varied strongly in thickness due to this deposition pattern, but covered a range from 100 s nm to greater than 50 μm.

The deposited layers were found to have a mixed grain structure, with finer grains close to the substrate and larger

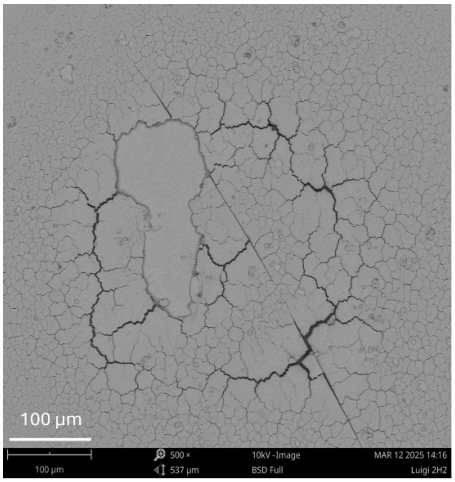

(a) M(P)H2

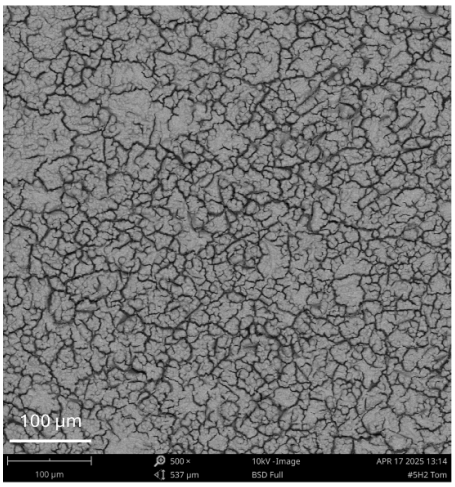

(b) M(R)H2

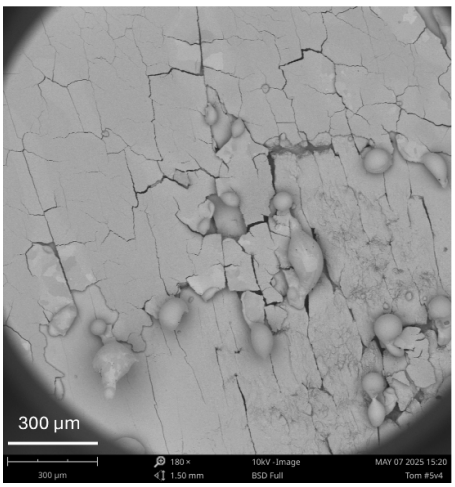

(c) M(P)v4

Figure 17. SEM images of targets (*a*) M(P)H2, (*b*) M(R)H2 and (*c*) M(P)v4 after simultaneous D-plasma and ELM-like loading.

columnar grains further away. This can be associated to Zone T growth in the Thornton structural zone model [24] and is similar in structure to layers grown by laboratory methods (magnetron sputtering and PLD) under similar conditions of pressure and temperature [17–21, 47]. The layers were harder, and with smaller crystallite domain size than bulk tungsten [48], but again in line with literature values for W thin films [17, 18, 20, 22, 23]. This helps to validate that studies using such films may be representative of in-situ grown layers. The layers were determined to be predominantly W, with low oxygen concentration ($\leqslant 5$ at.%), but potentially with a low (5–10 at.%) concentration of Mo, although results here are not conclusive.

Deposited layers were observed to sometimes flake off during the deposition process, with the process typically initiating at corners or other discontinuities. The flaking was strongly correlated to the surface roughness of the targets, with rough surfaces leading to much better adhesion than polished ones. This was determined to be related to the rate of production of nodal growth flaws in the material, as the rough structures produced many more of these which led to discontinuities in the coating which reduced stresses. High deposition rates were also found to be more likely to lead to flaking, while thick layers above around 20 μm thickness also showed flaking. This can be related to the generated tensile stress in the material which is large if either deposition rate or grain size (linked to thickness) is large, following the model of Chason *et al* [52]. In WEST deposited layers which were still attached were observed up to 55 μm thick [12]. The fact that layers were still adhered implies that residual stresses in the layers were much smaller than here, which could possibly arise from the more layered or mixed material nature of the deposits in WEST. Which layers are most representative for ITER requires further evaluation.

ELM-like loading of the W deposited layers by pulsed laser with simultaneous deuterium plasma deposition lead to the formation of crack networks in the coating, and in some cases extended also into the bulk where the coating was thin or well adhered to the substrate. In some cases flaking occurred at the laser spot location which was correlated mainly to the substrate being polished rather than rough, in line with observations of the spontaneous flaking behavior. Flaking occurred on polished samples for layer thicknesses greater than 1450 nm, while layers up to 7880 nm did not show flaking on rough samples. Some melted blobs also formed on poorly adhered edges of flaking coatings on polished samples due to the laser loading.

For ITER the deposition rates studied here are at the upper end of what may be expected based on the extrapolation given in section 1. Additionally the ITER divertor surfaces are planned to have a technical finish which will be close to the roughness of the sandblasted rough surfaces studied here. Both these facts indicate that the risk of flaking may be relatively low. However, tungsten layers of 10's of μm thickness could still build up over time and generate sufficient residual stresses that flaking may occur. Additionally for relatively small ELM-sizes and cycle numbers based on the results here, flaking may still be generated from initially attached deposits. Additionally several parameters are not matched with expectations of ITER operation, including the use of Ar plasma, rather than hydrogen isotopes, helium and seeding impurities as the real expected species mix. Physical sputtering and prompt-redeposition

did not take place during our exposure conditions, unlike in ITER where this may occur during both steady-state plasma and during ELM loading. Additionally eroded boron from the planned boronization process [1] may play a strong role in the formation and properties of the deposits by forming mixed layers, and is not yet considered in these studies. Studies on this topic should therefore aim to incorporate these factors in the future.

Acknowledgments

DIFFER is part of the institutes organisation of NWO. We acknowledge the support of the Magnum-PSI Facility Team at DIFFER. The Magnum-PSI facility at DIFFER has been funded by the Netherlands Organisation for Scientific Research (NWO) and EURATOM. This work has been carried out within the framework of the EUROfusion Consortium, funded by the European Union via the Euratom Research and Training Programme (Grant Agreement No 101052200 - EUROfusion). Views and opinions expressed are however those of the author(s) only and do not necessarily reflect those of the European Union or the European Commission. Neither the European Union not the European Commission can be held responsible for them.

Credit author statement

T.W. Morgan: Conceptualization, Methodology, Investigation, Resources, Writing—Original Draft, Visualization, Supervision, Project Administration, Funding Acquisition. **L.J. Bouwmeester**: Investigation, Methodology, Writing—Original Draft, Visualization. **L. Bana**: Investigation, Writing—Review & Editing, Visualization. **M.J.H. Cornelissen**: Methodology, Investigation, Writing—Review & Editing, Visualization. **M. Rasinski**: Investigation, Resources. **E. Zoethout**: Investigation, Writing—Review & Editing. **J.A.G. van Kesteren**: Investigation, Writing—Review & Editing. **C.J.D. Robben**: Investigation. **V. Mathayan**: Investigation. **S. Brons**: Methodology. **L.C.A. van Breemen**: Investigation. **D. Dellasega**: Investigation, Supervision, Writing—Review & Editing, Resources. **M. Passoni**: Supervision, Resources. **N. Lecis**: Investigation, Resources.

ORCID iDs

T.W. Morgan 0000-0002-5066-015X
L. Bana 0009-0003-1612-178X
M. Rasinksi 0000-0001-6277-4421
C.J.D. Robben 0009-0004-2040-4149
L.C.A. van Breemen 0000-0002-0610-1908
D. Dellasega 0000-0002-7389-9307
M. Passoni 0000-0002-7844-3691

References

[1] Pitts R.A. *et al* 2025 Plasma-wall interaction impact of the ITER re-baseline *Nucl. Mater. Energy* **42** 101854
[2] Schmid K. and Wauters T. 2024 Assessment of expected W erosion and implications of boronization on fuel retention *Nucl. Mater. Energy* **41** 101789
[3] Baron-Wiechec A., Fortuna-Zaleśna E., Grzonka J., Rubel M., Widdowson A., Ayres C., Coad J.P., Hardie C., Heinola K. and Matthews G.F. (JET Contributors) 2015 First dust study in JET with the ITER-like wall: sampling, analysis and classification *Nucl. Fusion* **55** 113033
[4] Fortuna-Zaleśna E., Grzonka J., Rubel M., Garcia-Carrasco A., Widdowson A., Baron-Wiechec A. and Ciupiński L. (JET Contributors) 2017 Studies of dust from JET with the ITER-like wall: composition and internal structure *Nucl. Mater. Energy* **12** 582–7
[5] Endstrasser N., Rohde V., Balden M., Humrickhouse P., von Toussaint U., Braams B.J., Chung H.-K. and Neu R. (the ASDEX Upgrade Team) 2011 Comparative study of the dust particle population sampled during four consecutive campaigns in full-tungsten ASDEX Upgrade *Phys. Scr.* **2011** 014021
[6] Balden M., Endstrasser N., Humrickhouse P., Rohde V., Rasinski M., von Toussaint U., Elgeti S. and Neu R. (the ASDEX Upgrade Team) 2014 Collection strategy, inner morphology and size distribution of dust particles in ASDEX Upgrade *Nucl. Fusion* **54** 073010
[7] Brochard F., Rohde V., Lunt T., Suárez López G., Shalpegin A. and Neu R. 2019 Intrinsic dust transport in ASDEX upgrade studied by fast imaging *Nucl. Mater. Energy* **18** 268–74
[8] Pan H., Ding R., Peng J., Yan R., Zhu D. and Chen J. 2022 Characterization of dust produced during the 2021 first campaign in EAST tokamak *Nucl. Mater. Energy* **33** 101251
[9] Arnas C. *et al* 2017 Characterization and origin of large size dust particles produced in the Alcator C-Mod tokamak *Nucl. Mater. Energy* **11** 12–19
[10] Arnas C. *et al* 2023 Micron-sized dust and nanoparticles produced in the WEST tokamak *Nucl. Mater. Energy* **36** 101471
[11] Gaspar J. *et al* 2024 Thermal and statistical analysis of the high-Z tungsten-based UFOs observed during the first deuterium high fluence campaign of the WEST tokamak *Nucl. Mater. Energy* **41** 101745
[12] Martin C. *et al* 2024 Post-mortem analysis of the deposit layers on the lower divertor after the 2023 high particle fluence campaign of WEST *Nucl. Mater. Energy* **41** 101764
[13] Sertoli M. *et al* 2015 Impact of W events and dust on JET-ILW operation *J. Nucl. Mater.* **463** 837–41
[14] Cornelissen M.J., Vernimmen J.W., Verstappen J.D., Zoethout E., Classen I.G., Beckers J. and Morgan T.W. 2024 Erosion enhancement by impurity entrainment in the highly collisional plasmas of Magnum-PSI *Nucl. Fusion* **65** 026009
[15] Rosanvallon S. *et al* 2009 Dust limit management strategy in tokamaks *J. Nucl. Mater.* **390–391** 57–60
[16] Romazanov J. *et al* 2022 Beryllium erosion and redeposition in ITER H, He and D-T discharges *Nucl. Fusion* **62** 036011
[17] Sun H.L., Song Z.X., Guo D.G., Ma F. and Xu K.W. 2010 Microstructure and mechanical properties of nanocrystalline tungsten thin films *J. Mater. Sci. Technol.* **26** 87–92
[18] Gordillo N., Panizo-Laiz M., Tejado E., Fernandez-Martinez I., Rivera A., Pastor J.Y., Castro C.G.d., del Rio J., Perlado J.M. and Gonzalez-Arrabal R. 2014 Morphological and microstructural characterization of nanostructured pure α-phase W coatings on a wide thickness range *Appl. Surf. Sci.* **316** 1–8
[19] t Hoen M.H.J., Dellasega D., Pezzoli A., Passoni M., Kleyn A.W. and Zeijlmans van Emmichoven P.A. 2015

Deuterium retention and surface modifications of nanocrystalline tungsten films exposed to high-flux plasma *J. Nucl. Mater.* **463** 989–92
[20] Ogorodnikova O.V., Ruset C., Dellasega D., Pezzoli A., Passoni M., Sugiyama K., Gasparyan Y. and Efimov V. 2018 Deuterium retention in dense and disordered nanostructured tungsten coatings *J. Nucl. Mater.* **507** 226–40
[21] Dellasega D., Merlo G., Conti C., Bottani C.E. and Passoni M. 2012 Nanostructured and amorphous-like tungsten films grown by pulsed laser deposition *J. Appl. Phys.* **112** 084328
[22] Mukherjee S. 2019 Thin film deposition from dual ion beam sputtering system *CSI Trans. on ICT* **7** 99–104
[23] Vüllers F.T.N. and Spolenak R. 2015 Alpha- vs. beta-W nanocrystalline thin films: a comprehensive study of sputter parameters and resulting materials' properties *Thin Solid Films* **577** 26–34
[24] Thornton J.A. 1977 High rate thick film growth *Annu. Rev. Mater. Sci.* **7** 239–60
[25] Arnell R.D. and Kelly P.J. 1999 Recent advances in magnetron sputtering *Surf. Coat. Technol.* **112** 170–6
[26] Pitts R. *et al* 2019 Physics basis for the first ITER tungsten divertor *Nucl. Mater. Energy* **20** 100696
[27] Corre Y. *et al* 2023 Testing of ITER-grade plasma facing units in the WEST tokamak: Progress in understanding heat loading and damage mechanisms *Nucl. Mater. Energy* **37** 101546
[28] Eich T., Sieglin B., Thornton A., Faitsch M., Kirk A., Herrmann A. and Suttrop W. 2017 ELM divertor peak energy fluence scaling to ITER with data from JET, MAST and ASDEX upgrade *Nucl. Mater. Energy* **12** 84–90
[29] Van Eck H. *et al* 2019 High-fluence and high-flux performance characteristics of the superconducting Magnum-PSI linear plasma facility *Fusion Eng. Des.* **142** 26–32
[30] Kajita S., Morgan T., Tanaka H., Hayashi Y., Yoshida N., Nagata D., Vernimmen J., Feng S., Zhang R. and Ohno N. 2021 Accelerated/reduced growth of tungsten fuzz by deposition of metals *J. Nucl. Mater.* **548** 152844
[31] Behrisch R. and Eckstein W. 2007 *Sputtering by Particle Bombardment* (*Topics in Applied Physics*) vol 110 (Springer) (available at:http://link.springer.com/10.1007/978-3-540-44502-9)
[32] Thompson M.W. 1986 The velocity distribution of sputtered atoms *Nucl. Instrum. Methods Phys. Res. B* **18** 411–29
[33] Eckstein W. 2002 *Calculated Sputtering, Reflection and Range Values IPP 9/132 Max-Planck-Institut für Plasmaphysik*
[34] Meiden H.J.V.D. *et al* 2013 Laser-based diagnostics applications for plasma-surface interaction studies *J. Instrum.* **8** C11011
[35] Morgan T.W., Balden M., Schwarz-Selinger T., Li Y., Loewenhoff T.H., Wirtz M., Brezinsek S. and De Temmerman G. 2020 ITER monoblock performance under lifetime loading conditions in Magnum-PSI *Phys. Scr.* **T171** 014065
[36] Mayer M. 1997 SimNRA Users Guide (available at: https://mam.home.ipp.mpg.de/Report%20IPP%209-113.pdf)
[37] Barradas N.P. and Jeynes C. 2008 Advanced physics and algorithms in the IBA datafurnace *Nucl. Instrum. Methods Phys. Res. B* **266** 1875–9
[38] Patterson A.L. 1939 The Scherrer formula for x-ray particle size determination *Phys. Rev.* **56** 978–82
[39] Oliver W.C. and Pharr G.M. 1992 An improved technique for determining hardness and elastic modulus using load and displacement sensing indentation experiments *J. Mater. Res.* **7** 1564–83
[40] Oliver W.C. and Pharr G.M. 2004 Measurement of hardness and elastic modulus by instrumented indentation: advances in understanding and refinements to methodology *J. Mater. Res.* **19** 3–20
[41] Morgan T., Li Y., Balden M., Brezinsek S. and De Temmerman G. 2021 Combined high fluence and high cycle number transient loading of ITER-like monoblocks in Magnum-PSI *Nucl. Fusion* **61** 116045
[42] Loewenhoff T., Linke J., Pintsuk G. and Thomser C. 2012 Tungsten and CFC degradation under combined high cycle transient and steady state heat loads *Fusion Eng. Des.* **87** 1201–5
[43] Cornelissen M.J. *et al* 2024 High erosion and re-deposition rates of tungsten in the highly collisional plasmas of Magnum-PSI *Nucl. Fusion* **65** 026008
[44] Manova D., Gerlach J.W. and Mändl S. 2010 Thin film deposition using energetic ions *Materials* **3** 4109–41
[45] Tanaka H., Hayashi Y., Kajita S., van der Meiden H.J., Yoshikawa M., Vernimmen J.W.M., Scholten J., Classen I., Morgan T.W. and Ohno N. 2020 Cross-field transport in detached helium plasmas in Magnum-PSI *Plasma Phys. Control. Fusion* **62** 115021
[46] Costin C., Mihaila I., van der Meiden H.J., Tanaka H., Scholten J. and van Eck H.J.N. 2023 Plasma rotation and axial flow velocities in Magnum-PSI from cross-correlation measurements *Plasma Sources Sci. Technol.* **32** 075010
[47] Paris P., Jögi I., Piip K., Passoni M., Dellasega D., Grigore E., Arnoldbik W.M. and van der Meiden H. 2021 In-situ LIBS and NRA deuterium retention study in porous W-O and compact W coatings loaded by Magnum-PSI *Fusion Eng. Des.* **168** 112403
[48] Warlimont H. and Martienssen W. (eds) 2018 *Springer Handbook of Materials Data*, (Springer)
[49] Sala M., Uccello A., Dellasega D., Pedroni M., Vassallo E. and Passoni M. 2020 Exposures of bulk W and nanostructured W coatings to medium flux D plasmas *Nucl. Mater. Energy* **24** 100779
[50] Dulmaa A., Cougnon F.G., Dedoncker R. and Depla D. 2021 On the grain size-thickness correlation for thin films *Acta Mater.* **212** 116896
[51] Hoffman R.W. 1976 Stresses in thin films: the relevance of grain boundaries and impurities *Thin Solid Films* **34** 185–90
[52] Chason E., Shin J.W., Hearne S.J. and Freund L.B. 2012 Kinetic model for dependence of thin film stress on growth rate, temperature and microstructure *J. Appl. Phys.* **111** 083520
[53] Engwall A.M., Rao Z. and Chason E. 2016 Origins of residual stress in thin films: interaction between microstructure and growth kinetics *Mater. Des.* **110** 616–23
[54] Bull S.J. and Berasetegui E.G. 2006 An overview of the potential of quantitative coating adhesion measurement by scratch testing *Tribol. Int.* **39** 99–114